



Cite this: *J. Mater. Chem. A*, 2015, **3**, 23230

Polymer-templated synthesis of hollow Pd–CeO₂ nanocomposite spheres and their catalytic activity and thermal stability†

Chenhao Du, Yun Guo, Yanglong Guo, Xue-qing Gong and Guanzhong Lu*

Developing methods for the fabrication of active and thermally stable noble metal/metal oxide nanomaterials are very important for catalysis and material fields. Herein, we used a polymer-template synthesis approach to prepare hollow Pd–CeO₂ nanocomposite spheres (NCSs) with Pd nanoparticles evenly distributed inside the CeO₂ shell, in which the aggregation of Pd nanoparticles can be well inhibited with the help of the protection of CeO₂ nanocrystallites even after being calcined at 700 °C. The Pd nanoparticles are partially buried in the CeO₂ shell and the surface Pd species are highly ionic, which is caused by the electron exchange at the Pd–CeO₂ interface during calcination. This hollow structure Pd–CeO₂ nanocatalyst shows excellent catalytic activity and stability in the aqueous selective reduction of 4-nitrophenol and gaseous CO oxidation. For the selective reduction of 4-nitrophenol, the reaction rate of this h-Pd–CeO₂ NCS catalyst compared to those of the supported Pd/CeO₂ and physically mixed Pd + CeO₂ catalysts is almost 14 times and 5 times faster, respectively. For the CO oxidation, the larger Pd–CeO₂ interface in h-Pd–CeO₂ NCSs could facilitate the reaction between the adsorbed CO and O₂, thus showing better low temperature activity. This paper emphasizes the advantages of a core-shell hollow structure and provides a new way for obtaining novel functional nanocatalysts.

Received 7th July 2015
Accepted 8th October 2015

DOI: 10.1039/c5ta05092h

www.rsc.org/MaterialsA

1. Introduction

Noble metal nanoparticles (NPs) have been extensively researched in the field of catalysis in recent years, due to their highly effective catalytic performance.^{1–3} It is well known that the catalytic activity of noble metal NPs is closely dependent on their composition, size, shape and crystallinity.^{4–7} However, owing to their high surface area and surface energy, noble metal NPs tend to aggregate to larger particles to minimize their surface energy, especially during the catalytic reaction at high temperature, which could easily lead to their deactivation or loss of the catalytic activity.^{8,9} To solve these problems, isolation of noble metal NPs in small cavities is a reasonable solution, because it can efficiently prevent particle migration and its

deactivation. Besides, this isolation method can also reduce the leaching of the active components from the catalyst particles in the chemical process, which is another important aspect in the design of new nanocatalysts.^{10,11}

To isolate noble metal NPs, porous inert oxide coatings and core-shell hollow nanostructures are the ideal solution approaches, and both have been widely researched recently.^{12–20} Lu *et al.* designed a coking- and sintering-resistant palladium catalyst by an atomic layer deposition method, which can enhance the catalytic activity and stability of the Pd/Al₂O₃ catalyst for the oxidative dehydrogenation of ethane.¹⁸ Zhang *et al.* reported the graphene nanosheet-supported ultrafine metal nanoparticles encapsulated by thin mesoporous SiO₂ layers, which exhibited remarkable high-temperature stability.¹⁹ Similarly, porous silica-coated Pt NPs on carbon nanotubes possessed good thermal stability for the hydrogenation of nitrobenzene.²⁰ However, Al₂O₃ or SiO₂ are unreactive components and only play a dispersion role, and the synergistic effect between noble metal NPs and the Al₂O₃ or SiO₂ layer is quite weak. From a viewpoint of heterogeneous catalysis, especially for metal/metal oxide catalysts, the interaction between the metal nanoparticles and the reactive support,^{21–23} such as CeO₂ and TiO₂, is quite vital for improving the reactivity and stability of the catalysts.

As one of the most commonly used reducible oxides, ceria possesses a high oxygen storage capacity and redox property,

Key Laboratory for Advanced Materials, Research Institute of Industrial Catalysis, East China University of Science and Technology, Shanghai 200237, P. R. China. E-mail: gzhlu@ecust.edu.cn; Fax: +86-21-64252923

† Electronic supplementary information (ESI) available: TEM images: Pd NPs and their size distribution (Fig. S1); Pd NPs on resin polymer spheres (Fig. S2); h-Pd–CeO₂ NCSs treated with NaBH₄ and then N₂ at 650 °C (Fig. S6), after being used in reduction of 4-NP (Fig. S10) and CO oxidation (Fig. S11); a mixture of Pd + CeO₂ (Fig. S7); Pd/CeO₂-imp (Fig. S8). XPS spectra: h-Pd–CeO₂ NCSs (Pd 3d, Fig. S5) and Pd/CeO₂-imp (Pd 3d, Fig. S9); h-Pd–CeO₂ NCSs and Pd/CeO₂-imp (O 1s, Fig. S12). TG curves and EDS line-scanning profiles of h-Pd–CeO₂ NCSs (Fig. S3 and S4). Textural properties and crystallite sizes of catalysts (Table S1). See DOI: 10.1039/c5ta05092h



and plays an important role in the field of catalysis and has been researched extensively.^{24–27} Although various methods for the fabrication of hollow ceria spheres have been reported,^{28–30} the research on CeO₂-containing nanocomposite hollow spheres, especially composites with noble metal nanoparticles, is relatively rare. For example, Liu and co-workers designed a nano-reactor with noble metal NPs decorated in the inner walls of the CeO₂ shells and showed that it could enhance the catalytic activity and stability.³¹ Xu *et al.* synthesized hollow Pd@CeO₂ spheres by a core-shell protocol, which exhibited excellent reusable and higher catalytic performance for the thermocatalytic and photocatalytic selective reduction of aromatic nitro compounds.³² However, these research studies were only involved with the catalytic processes under ambient conditions, and the high-temperature stability of these catalysts was not demonstrated, which is very important for the gas-solid phase catalytic reaction at a higher temperature. Therefore it is quite necessary to develop novel nanocatalysts with good activity and stability for both gas- and liquid-phase reactions.

Herein, we reported the fabrication of hollow Pd–CeO₂ nanocomposite spheres (NCSs) by a facile hard-template method in an aqueous phase, followed by the elimination of the polymer templates by simple calcination. In these hollow Pd–CeO₂ NCSs, the aggregation of Pd nanoparticles can be efficiently avoided by the protection of the CeO₂ crystal. The high dispersity of Pd species can be well maintained even after calcination at 700 °C. The synthesized hollow Pd–CeO₂ NCSs exhibit high catalytic activity for the selective reduction of aromatic nitro compounds under ambient conditions and CO oxidation. It is most important that hollow Pd–CeO₂ NCSs possess high thermal stability and reusability compared to conventionally supported Pd/CeO₂ catalysts.

2. Experimental section

2.1. Preparation of samples

Monodispersed resorcinol-formaldehyde (RF) polymer spheres. RF polymer spheres were synthesized.³³ Typically, 0.1 mL of ammonia aqueous solution (NH₄OH, 25 wt%) was mixed with a solution containing 8 mL of ethanol and 20 mL of de-ionized water. After stirring for 1 h, 0.1 g of resorcinol was added to this mixed solution and it was continually stirred for 30 min. Then 0.14 mL of formaldehyde solution was added and stirred for 24 h at 30 °C, and subsequently this synthesized solution was transferred to a Teflon-lined stainless autoclave and treated at 100 °C for 24 h. The as-synthesized product was collected by centrifugation and washed with de-ionized water twice. Finally, the solid product was dried in air at 100 °C for 24 h.

PVP-protected Pd nanoparticles. PVP-protected Pd nanoparticles were prepared by the alcohol reduction method.³⁴ H₂PdCl₄ aqueous solution (2 mM) was prepared by mixing 106.4 mg of PdCl₂, 6 mL of 0.2 M HCl and 294 mL of ultrapure water. A mixed solution of 15 mL H₂PdCl₄ aqueous solution, 21 mL de-ionized water, 14 mL ethanol and 66.7 mg PVP was refluxed in a 100 mL flask at 90 °C for 3 h. The obtained dark-brown PVP-

protected Pd colloidal solution was stable at room temperature for months.

Hollow Pd–CeO₂ nano-composites (h-Pd–CeO₂). 25 mg of as-prepared RF spheres was dispersed in 20 mL of de-ionized water under ultra-sonication to obtain a homogeneous dispersion, followed by adding the Pd colloidal solution (10–15 μmol). This mixture was stirred for 4–6 h to allow Pd NPs fully deposited on the surface of RF spheres to form an RF@Pd structure. Then a mixed solution of 0.15 g of CeCl₃, 0.085 g of hexamethylenetetramine (HTMA) and 20 mL of de-ionized water was added into the solution containing RF@Pd particles mentioned-above, and it was continually stirred for 15 min. Then this synthesized solution was transferred into a 100 mL Teflon-lined stainless autoclave and treated at 100 °C for 6 h. The obtained products were separated by centrifugation, washed with de-ionized water 3 times to remove unreacted residues, and then dried at 60 °C overnight and calcined at 500–700 °C for 2 h in a muffle furnace.

The Pd/CeO₂ catalyst. The supported Pd/CeO₂ catalyst was prepared by the conventional impregnation method (Pd/CeO₂-imp), and the Pd loading was ~2.0 wt%. Commercial CeO₂ powder was provided by Aladdin Company. The as-synthesized Pd/CeO₂ powder was calcined at 500 °C for 2 h.

The physical mixture of Pd + CeO₂. The 2.0 wt% Pd physically mixed sample was prepared by an evaporation of the colloidal solution including CeO₂ nanoparticles and Pd nanoparticles and followed by calcination in air at 500 °C for 2 h.

2.2. Catalytic activity testing

The selective reduction of 4-nitrophenol. Catalytic performance of the catalyst for the selective reduction of 4-nitrophenol was tested as follows. Typically, the catalyst (1.5 mg) was added into 40 mL of ultrapure water in a 100 mL beaker to form a homogeneous dispersion under ultrasonication for 10 min, and then 0.5 mL of freshly prepared 0.5 M NaBH₄ aqueous solution was added. After stirring for a few seconds at room temperature, 4-nitrophenol (0.012 M, 0.25 mL) was added into the reactor at room temperature (25 °C). The reaction process was monitored by the direct color change of the solution. At different reaction times, 1.5 mL of the solution was withdrawn with a syringe and filtered using a 0.22 μm Millipore film, and the reaction solution was analyzed by UV-Vis spectroscopy.

Recycling of the catalyst. After the reaction ended, the catalyst was separated by centrifugation at 5000 rpm for 10 min, and the catalyst was dried at 60 °C. Then this catalyst was directly reused under the same reaction conditions.

CO oxidation. The catalytic activity of the sample for CO oxidation was evaluated at atmospheric pressure in a quartz tubular reactor. 30 mg of the catalyst was mixed with 200 mg of silica (40–60 mesh). The total flow rate of the feed gas of 1% CO–20% O₂/N₂ was 50 mL min^{−1}. The catalyst was pretreated in N₂ at 150 °C for 1 h and then the temperature was raised at a rate of 2 °C min^{−1}. The gas composition was monitored online using a gas chromatograph (GC 2060 system) with a flame ionization detector (FID) and methanation reactor. The conversion of CO was calculated on the basis of the change of CO concentrations in the inlet and outlet gases.



2.3. Characterization of samples

Elemental analysis of the sample was done by inductively coupled-plasma atomic emission spectroscopy (ICP-AES) on a Varian 710ES instrument (Varian Co. Palo Alto, US). Powder X-ray diffraction (XRD) patterns were recorded on a PANalytical PW 3040/60 X'Pert Pro powder diffractometer with CuK α radiation, which was operated at 40 kV and 40 mA and the scanning speed was 0.5° min⁻¹. Thermogravimetric (TG) analysis was conducted on a Pyris diamond thermal analyzer at a heating rate of 10 °C min⁻¹ from room temperature to 800 °C. The surface areas of samples were measured by N₂ adsorption/desorption isotherms at -196 °C on a Micromeritics ASAP 2020 instrument, and calculated by the Brunauer–Emmett–Teller (BET) method.

Transmission electron microscopy (TEM) images and energy dispersive X-ray spectroscopy (EDX) spectra were obtained with JEM-1400 & JEM-2100 transmission electron microscopes, respectively. The sample was ultrasonically suspended in the ethanol solvent, and one or two drops of this slurry was deposited on a copper grid. The liquid phase was evaporated before the grid was loaded into the microscope. Scanning electron microscopy (SEM) images were taken on a Hitachi S-3400 scanning electron microscope operated at 15 kV and using secondary electrons to form the images. The sample was coated with a thin layer of gold before testing.

X-ray photoelectron spectroscopy (XPS) spectra of the samples were obtained on a Kratos Axis Ultra DLD photoelectron spectrometer equipped with AlK α (1486.6 eV) radiation as the excitation source. All binding energies (BE) were determined with respect to the C 1s line (284.6 eV) originating from adventitious carbon.

3. Results and discussion

3.1. Preparation of hollow Pd–CeO₂ nanocomposite spheres and their properties

The synthesis process of hollow Pd–CeO₂ nanocomposite spheres (NCSs) is illustrated in Scheme 1. The pre-synthesized Pd colloidal nanoparticles (NPs) with PVP as the stabilizer are 2.5–3 nm (Fig. S1†), and could be loaded on the surface of monodispersed resin polymer spheres by the π – π interaction between the polymer template and PVP (Fig. S2†).^{32,35} Basically, almost all of the Pd colloidal nanoparticles are successfully deposited on the surface of the polymer, which can be verified by the relative colorless transparent supernatant obtained after centrifugation of the RF@Pd suspension. As is well known, hexamethylenetetramine (HTMA) can hydrolyze in water to give NH₃,³⁶ while the basicity of the solution is slowly changed

during the reaction, which ensures the slow hydrolysis of CeCl₃ and condensation of Ce³⁺ ions. Meanwhile, with the coordination effect of PVP and surface functional groups on the polymer surface, CeO₂ could be well deposited on the template surface to form an RF@Pd@CeO₂ core-shell structure. Followed by calcination in air, the RF template and PVP are removed and the hollow CeO₂ shell forms simultaneously.

As shown in Fig. 1, the diameter of mono-dispersed RF resin polymer spheres is ~500 nm, and the well-structured hollow spheres and the inner hollow structure can be clearly observed as indicated with the arrows (Fig. 1b), which is further confirmed by the TEM image (Fig. 1c). The CeO₂ shells composed of sub-10 nm CeO₂ nanocrystallites with the thickness of ~35 nm, and the cavities in the shell can guarantee the reagents diffusion and contact in the inner and outer surfaces of the shell during the catalytic reaction. No bare Pd NPs are spotted on the surface of hollow spheres and almost all of the Pd NPs are embedded in the CeO₂ nanocrystals after calcination, forming Pd–CeO₂ interfaces as indicated by the white arrow (Fig. 1d). The TG analysis shows that the hollow Pd–CeO₂ NCSs exhibit hardly weight loss at 100–800 °C, which demonstrates the complete elimination of resin polymer spheres during the calcination (Fig. S3†).

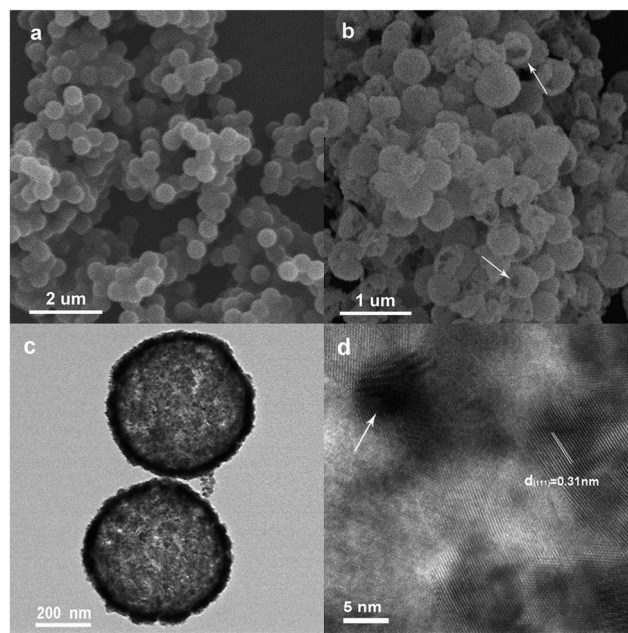
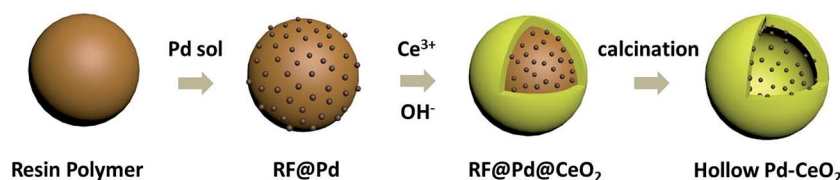


Fig. 1 SEM images of (a) resin polymer template and (b) SEM, (c) TEM, and (d) HR-TEM of hollow Pd–CeO₂ NCSs calcined at 773 K.



Scheme 1 The formation process of hollow Pd–CeO₂ nano-composite spheres.



Owing to the high electron density of polycrystalline CeO_2 and the hollow shell structure, it is difficult to identify Pd NPs located on the ceria shell. To visualize the spatial distribution of Pd species, we used the EDX technique to analyze the individual hollow Pd– CeO_2 sphere, and the results are shown in Fig. 2. It can be seen that the elements of Pd, Ce and O spread evenly on the whole sphere, which proves that no Pd aggregation appeared on the CeO_2 shell. Besides, the composition line-scan profiles across a single h-Pd– CeO_2 nanocomposite sphere were obtained by means of SEM-EDX and are shown in Fig. S4,† which indicates that all the elements (Ce, O and Pd) are distributed throughout the sphere.

As shown in the XRD spectra (Fig. 3d), the hollow Pd– CeO_2 NCSs are the polycrystalline structures, the diffraction peaks result from CeO_2 , and no diffraction peaks of Pd or Pd oxide could be observed, probably due to the relatively low content or high dispersion of Pd species in the sample. With an increase in the calcination temperature from 500 to 700 °C, the hollow structure is well maintained and no Pd NPs or aggregated Pd particles were observed in its TEM images (Fig. 3a–c); the diffraction peaks become slightly narrower, while the size of CeO_2 crystallites increases from 5–10 to 10–15 nm and its BET surface area decreases from 59.3 to 33.9 $\text{m}^2 \text{g}^{-1}$ (Table S1†). As shown in Fig. 3b, the shell is more rugged and this hard-template method can effectively inhibit the growth of the crystal size at a higher temperature, whereas isolated CeO_2 nanoparticles would severely aggregate as indicated by the white arrow in Fig. 3a. Compared to the supported Pd/ CeO_2 catalyst (9.1 $\text{m}^2 \text{g}^{-1}$), the hollow Pd– CeO_2 NCSs have a larger surface area (33.9 $\text{m}^2 \text{g}^{-1}$) after calcination at 700 °C (Table S1†).

The hollow Pd– CeO_2 NCSs have also been investigated by the XPS technique, and the results are shown in Fig. 4. In the Pd

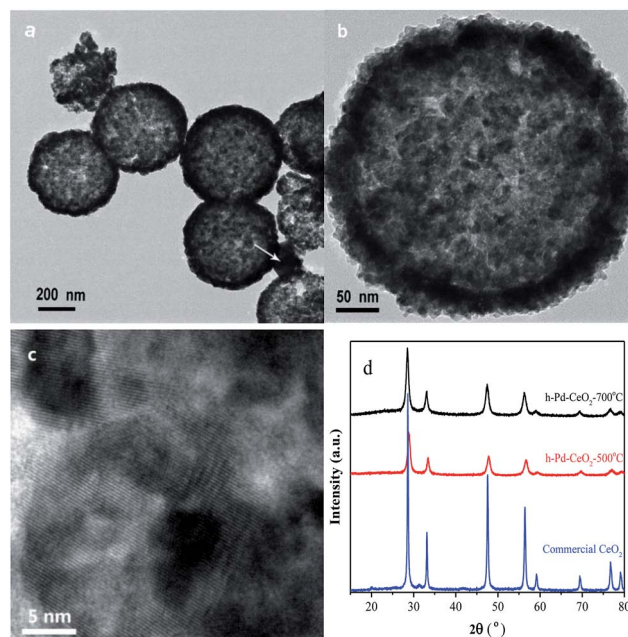


Fig. 3 (a–c) TEM images of hollow Pd– CeO_2 NCSs calcined at 700 °C and (d) XRD profiles of CeO_2 and h-Pd– CeO_2 NCSs.

$3d_{5/2}$ and $3d_{3/2}$ XPS spectra, two peaks are located at ~ 337.6 eV and 342.9 eV, respectively. In general, the BE (Binding Energy) values of Pd $3d_{5/2}$ in PdO species are in the range of 336–337.2 eV, so that the Pd in the hollow Pd– CeO_2 NCS should not be PdO. It was reported that, the fact that the XPS peaks of Pd^{2+} shifted to a higher BE value in Pd/ CeO_2 , could be explained by the formation of a solid solution-like $\text{Pd}_x\text{Ce}_{1-x}\text{O}_2$ structure, in which the Pd^{2+} ions replaced the Ce^{4+} ions in the CeO_2

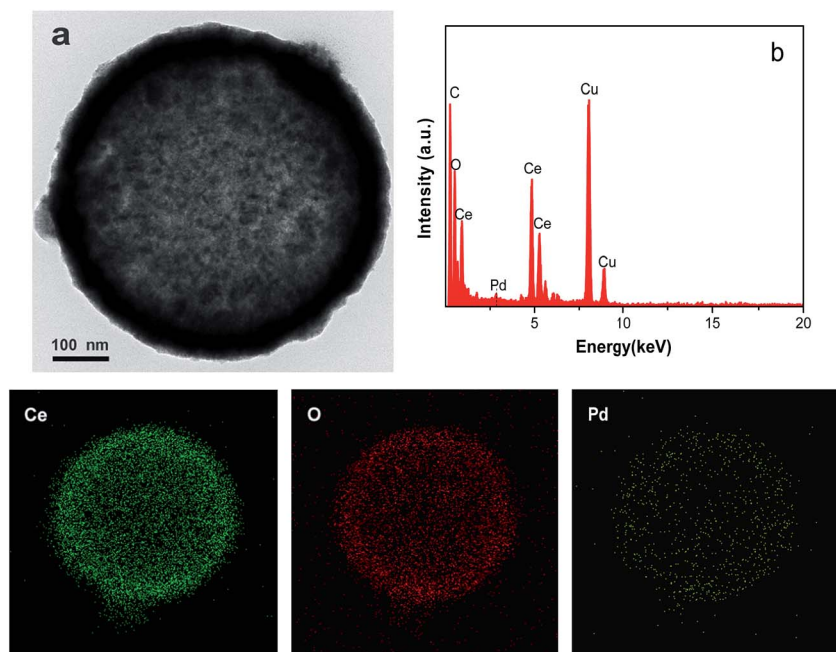


Fig. 2 (a) TEM images, (b) EDX spectra of individual hollow Pd– CeO_2 NCS calcined at 500 °C, and its elemental mappings of Ce, O and Pd.



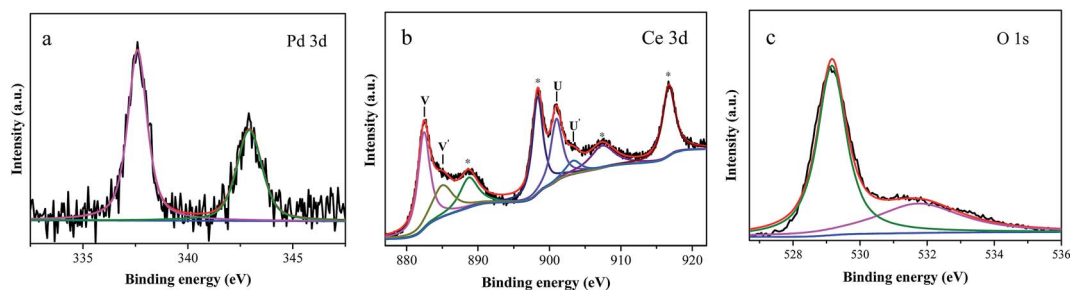


Fig. 4 XPS spectra of (a) Pd 3d, (b) Ce 3d and (c) O 1s for hollow Pd–CeO₂ NCSs.

crystalline lattice.^{37–40} This result demonstrates that the Pd NPs are embedded inside the CeO₂ nanocrystals, but not completely buried in the ceria shell. A fraction of Pd atoms located at the Pd–CeO₂ interface are exposed and the electron exchange between the Pd atoms and the CeO₂ matrix leads to the formation of ionic Pd species. Besides, previous research studies showed that the Pd²⁺ ions could not be completely reduced and a minor Pd²⁺ component might exist on the surface of Pd NPs.^{41,42} Thus, on the basis of XPS data and the Pd–CeO₂ interface observed in Fig. 1d, we can consider that the chemical state of surface Pd in the hollow Pd–CeO₂ NCSs is mainly ionic Pd²⁺ but not in the form of PdO, which probably results from the strong metal-support interaction caused by the treatment at high temperature, and forming the solid solution-like Pd_x–Ce_{1–x}O₂ structure.

For the Pd–CeO₂ NCS, after being calcined at 700 °C, its valence state of Pd species is unchanged, but the intensities of peaks are stronger than those of the sample calcined at 500 °C (Fig. S5†), which indicates that the surface concentration of Pd species increased after calcination at higher temperature (Table 1). This phenomenon is caused probably by two reasons. (1) Small Pd nanoparticles would undergo a structural evolution and the Pd atoms could dissociate from Pd nanoparticles in the process of calcination at 800 °C, but this situation would not occur at 500 °C.⁴³ Thus, in the h-Pd–CeO₂ NCSs, some Pd atoms may dissociate and be incorporated into the CeO₂ nanocrystallites during the calcination at 700 °C, which causes an increase in the concentration of surface Pd species, though the Pd NPs remain in their original places. (2) After calcination at 700 °C, the growth of CeO₂ nanocrystallites leads to the surface shrinkage of the ceria hollow sphere and a decrease in its surface area (from 59.3 to 33.9 m² g^{−1}, Table S1†). Thus the Pd NP number per square meter would increase, resulting in the

higher surface concentration of Pd species for the sample calcined at 700 °C than that of the sample calcined at 500 °C.

Fig. 4b shows the Ce 3d XPS spectrum of hollow Pd–CeO₂ NCSs, in which there are the V (BE = 882.5 eV) and U (901.0 eV) peaks, four (*) satellite peaks (BE = 888.8, 898.4, 907.4, and 916.7 eV) and the V' (885.2 eV) and U' (903.5 eV) peaks.⁴⁴ These results show that the main valence state of Ce in the hollow Pd–CeO₂ NCSs is +4 (V, U and four satellite peaks) with a small amount of Ce³⁺ (V' and U' peaks). In the O 1s spectra, the peaks at around 529.2 eV and 531.8 eV are ascribed to the lattice oxygen in the hollow Pd–CeO₂ NCSs and their surface oxygen species, respectively.

The amount of Pd obtained by ICP-AES in hollow Pd–CeO₂ NCSs was ~2.15%, and obviously higher than the theoretic value of Pd (1.5 wt%) in the synthesized solution (Table 1), indicating that not all Ce³⁺ ions in the solution were converted to CeO₂ in the synthesis process. For the sample calcined at 500 °C, the fact that the Pd content obtained by XPS is similar to that by ICP confirms that Pd evenly distributes in the sample. With an increase in the calcination temperature from 500 to 700 °C, the surface concentration of Pd increases from 2.0 to 4.3 wt% (by XPS), indicating that high temperature enriched Pd on the surface. For the supported Pd/CeO₂ catalyst, the surface concentration (6.0 wt%) of Pd is much higher than that of the Pd loading of 2.0 wt%.

The above-mentioned results show that by using resin polymer spheres as the hard template and with the help of the strong interaction between Pd and CeO₂, the sandwich-like RF polymer@Pd NP@CeO₂ core-shell structure materials can be efficiently converted to hollow Pd–CeO₂ nanocomposite spheres after simple calcination. CeO₂ nanocrystals are closely stacked around the well-dispersed Pd NPs on the shell, thus making the surface valence state of Pd highly ionic, rather than metallic. In

Table 1 Composition of hollow Pd–CeO₂ nanocomposite spheres and supported Pd/CeO₂ catalysts

Catalyst	Pd (wt%) in solution	XPS		ICP	
		Pd (wt%)	Pd/Ce (atom)	Pd (wt%)	Pd/Ce (atom)
h-Pd–CeO ₂ -773 K	1.5	2.00	0.032	2.15	0.035
h-Pd–CeO ₂ -873 K	1.5	2.76	0.045	1.95	0.032
h-Pd–CeO ₂ -973 K	1.5	4.30	0.065	1.95	0.032
Supported Pd/CeO ₂ -773 K	2.0	6.00	0.097	2.00	0.032



the high-temperature calcination process, no Pd aggregation was formed, which demonstrates the efficient shielding effect of shell CeO_2 crystals at higher temperatures.

3.2. Catalytic performance of hollow Pd– CeO_2 nanocomposite spheres

The catalytic activity of hollow Pd– CeO_2 NCSs was evaluated for the reduction of 4-nitrophenol (4-NP) to 4-aminophenol (4-AP) by an excess of NaBH_4 under ambient conditions and the oxidation of CO, which have been considered as the typical model reactions to investigate the catalytic activities of noble metal catalysts under aqueous or gaseous conditions.

It is well known that the 4-NP solution exhibits a strong absorption peak at 317 nm under a neutral or acid environment. However, with the excess of NaBH_4 in the solution, the 4-NP ions quickly become the dominant species due to the alkalinity of the solution and relatively higher acidity of 4-NP compared to water, thus leading to the H^+ dissociation from 4-NP to react with NaBH_4 , leaving the 4-NP anions. This is consistent with the peak shifting to 400 nm.

As shown in Fig. 5a, when a small amount of the catalyst (1.5 mg) was added to the solution, the absorption peak at 400 nm decreased quickly and a new peak at 295 nm appeared simultaneously, which indicates the reduction of 4-NP and formation of the 4-AP product. After ~ 2 min of the reaction, the absorption intensity at 295 nm reached a maximum and the absorption peak at 400 nm entirely diminished. Meanwhile, the light yellow solution completely faded and became colorless.

In the selective reduction of 4-NP to 4-AP, Pd acted as the primary active site to catalyze the reduction reaction by facilitating the electron transfer from BH_4^- to the reactant, thus leading to the effective reduction of the nitro group.⁴⁵ In order to clarify the chemical valence of Pd active sites in the reaction process, we performed one experiment without the 4-NP reactant, but only the excess NaBH_4 , in which other experiment conditions were maintained. The results show that when the hollow Pd– CeO_2 NCS catalyst was added to the solution under stirring for a few seconds, the color of this catalyst changed from brown to gray, which is caused by the reduction of Pd^{2+} to metallic Pd.

As shown in Fig. 6a, the XPS spectrum of the *in situ* reduced sample exhibits only two peaks at about 335.3 eV and 340.2 eV, indicating the formation of metallic Pd species by the reduction of partial Pd^{2+} ions. Therefore, we presume that the high catalytic activity of the hollow Pd– CeO_2 NCSs is attributed to these metallic Pd clusters on the surface of CeO_2 crystallites. Besides, the core-shell structural features can enhance the synergistic effect between the Pd NPs and the CeO_2 NPs and speed up the charge transfer rate, resulting in an increase in the catalytic activity.⁴⁶ To test the thermal-resistant stability of these h-Pd– CeO_2 NCSs, we further treated the reduced sample at 650 °C in N_2 for 4 h, and then its catalytic activity for the 4-NP reduction was tested under the same conditions. Compared to the catalytic activity of the fresh catalyst (Fig. 5b), after the sample was treated with NaBH_4 and then calcined at 650 °C in N_2 for 4 h, its catalytic activity remained unchanged (Fig. 5b), that is, the conversion of 4-NP to 4-AP could be completed in ~ 2 min. As shown in the TEM images of this reduced and thermally treated sample, its structure and shape could be well maintained (Fig. S6†), indicating the good chemical and thermal stability of this Pd– CeO_2 NCS catalyst.

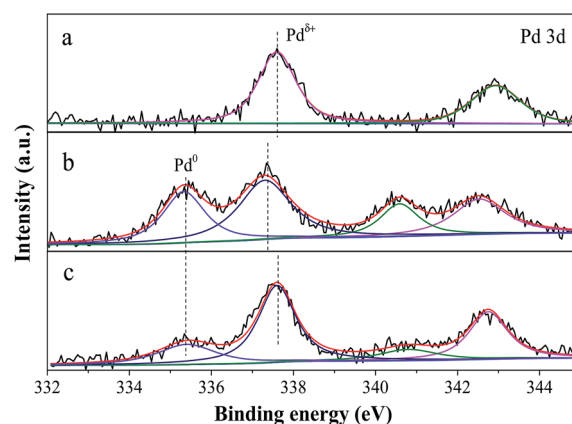


Fig. 6 Pd 3d XPS spectra of the hollow Pd– CeO_2 nanocomposite (a) calcined at 500 °C, (b) after being treated with NaBH_4 , and (c) after CO oxidation.

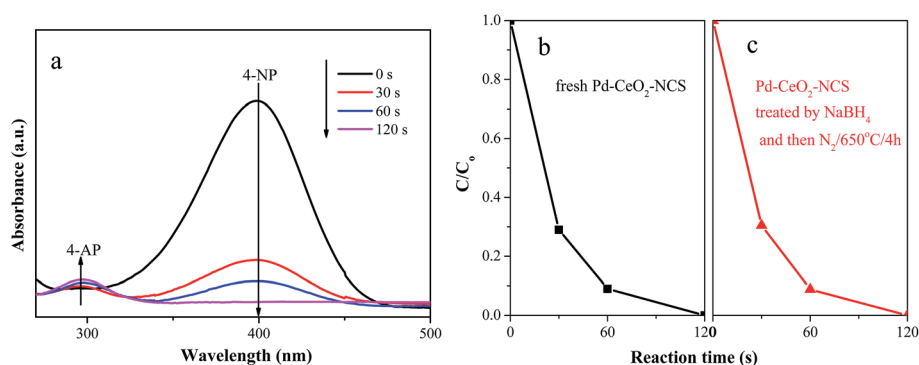


Fig. 5 (a) UV-Vis absorption spectra in the reduction of 4-NP to form 4-AP by an excess of NaBH_4 under ambient conditions over the hollow Pd– CeO_2 NCSs and (b and c) the concentration (C/C_0) of 4-NP as a function of the reaction time over (b) the fresh sample and (c) one treated with NaBH_4 and then calcined at 650 °C for 4 h in N_2 .



For a comparison, the catalytic activity of the Pd/CeO₂-imp catalyst prepared by the impregnation method and the physical mixture of the Pd + CeO₂ catalyst were also tested under the above-mentioned experiment conditions. The 4-NP conversion can be directly seen from the $\ln(C/C_0)$ (C is the concentration of 4-NP at the reaction time (t) and C_0 is the initial concentration of 4-NP) versus the reaction time (t), which is shown in Fig. 7. Evidently, the two reference catalysts possess inferior catalytic performance compared to that of the h-Pd-CeO₂ NCSs. For the reduction of 4-NP with an excess of NaBH₄, CeO₂ exhibits no catalytic activity. Therefore, the catalytic performances of these samples are strongly affected by the size of Pd nanoparticles and their states in the reaction system. As shown in the TEM image of Fig. S7,† for the physical mixture of the Pd + CeO₂ catalyst calcined at 500 °C without the purposeful design of the core-shell hollow structure, agglomeration of Pd nanoparticles occurs, thus, the available surface area of active Pd would decrease obviously, resulting in the reduction of its catalytic activity. As for the Pd/CeO₂-imp catalyst, though no bare Pd particles are seen in the TEM images, the Pd species are not evenly distributed on the whole CeO₂ support (Fig. S8†). The XPS analysis indeed exhibits a peak at 336.6 eV, which could be attributed to the formation of PdO species (Fig. S9†). Besides, most of the Pd/CeO₂-imp particles are severely sintered (Fig. S8†) and the sample cannot be well dispersed in 4-NP solution. The catalyst powder would quickly deposit at the bottom of the reaction vessel during the catalytic reaction, which limits the efficient contact between the reactants and the Pd sites in the solution, resulting in a remarkable reduction of its catalytic activity.

The above results show that the structures of the catalyst and active Pd states indeed affect their catalytic performances. Among the three catalysts, the Pd NPs in hollow Pd-CeO₂ NCSs could be well protected by CeO₂ nanocrystals in the shell, thereby preserving their high catalytic activity. And the porous CeO₂ shell and the hollow structure could favor the diffusion of the reactants and products, and increase the efficient contact between the reactants and the Pd active sites, leading to an

enhancement of the catalytic performance. TOF of the h-Pd-CeO₂ NCSs was calculated and reached 335 h⁻¹, which shows good catalytic activity compared to the catalysts reported (Table 2).

Fig. 8a shows the relationship of $\ln(C/C_0)$ versus the reaction time (t) over the h-Pd-CeO₂ NCS catalyst with different amounts. An almost linear evolution between $\ln(C/C_0)$ and time (t) indicates a first-order reaction for the concentration of 4-NP. When the catalyst amount is 1.5 mg (0.038 mg_{cat} mL⁻¹), the reduction rate of 4-NP is close to that over 2.2 mg of the catalyst (0.055 mg_{cat} mL⁻¹); decreasing the catalyst concentration would dramatically decrease the catalytic reaction rate, and further increasing the catalyst concentration hardly affects the catalytic reaction rate obviously, so the appropriate catalyst amount is about 0.038 mg_{cat} mL⁻¹. As shown in Fig. 7 and 8, the reduction of 4-NP to 4-AP by an excess of NaBH₄ under ambient conditions is of the first order reaction for 4-NP concentration, hence, the rate constant k can be calculated from the rate equation $\ln(C/C_0) = -kt$.

Fig. 8b shows the effect of the calcination temperature on the catalytic activity of the h-Pd-CeO₂ NCS catalyst. As shown in the plots of $\ln(C/C_0)$ versus the reaction time, the catalytic activity of this catalyst increases slightly after being calcined at 700 °C, this is because the surface concentration of Pd species was increased after calcination at higher temperature (Table 1). It is interesting to note that the Pd nanoparticles in the h-Pd-CeO₂ NCSs did not aggregate even after being calcined at 700 °C and their catalytic activity could be well maintained.

Fig. 8c shows the effect of recycling use on the catalytic activity of h-Pd-CeO₂ NCSs. With the increase of the recycling times, the conversion of 4-NP dropped gradually, and the conversion of 4-NP reached 84% after 6 times of recycling use. Notice that the h-Pd-CeO₂ NCS catalyst was reclaimed from the solution by centrifugation before reuse, in which some nanocomposites cannot be reclaimed due to their excellent dispersion in water, and only about 50% of h-Pd-CeO₂ NCSs could be obtained after 6 cycles. When this recovered catalyst was replenished to 1.5 mg by adding a fresh catalyst, its catalytic conversion can reach 100% once again in the 7th and 8th run. The TEM image (Fig. S10†) shows that the morphology of the Pd-CeO₂ NCSs after 5 times of recycling use could be well maintained, though some hollow spheres are broken, and the ICP analysis shows that their Pd amount is about 1.9 wt%, that is to say, almost no leaching of Pd species occurs after the recycling use of 5 times. These phenomena verify that it is the

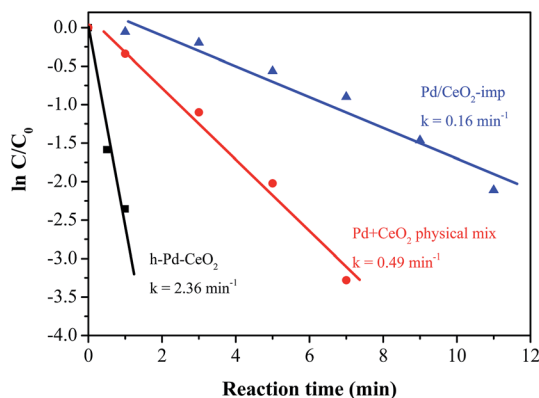


Fig. 7 $\ln(C/C_0)$ as a function of the reaction time (t) over hollow Pd-CeO₂ NCS, Pd/CeO₂-imp and Pd + CeO₂ physical mixture catalysts for the reduction of 4-NP to 4-AP by an excess of NaBH₄ under ambient conditions.

Table 2 TOF values over Pd-based nanocatalysts for the reduction of 4-NP

Catalyst	TOF (h ⁻¹)	Ref.
Pd/PPy/TiO ₂	32.3	47
Pd-spherical polyelectrolyte brushes	159	48
@Pd/CeO ₂	1068	31
Core-shell Pd@h-CeO ₂	300	32
Pd/polymer/CNT	96	49
h-Pd-CeO ₂	335	This work



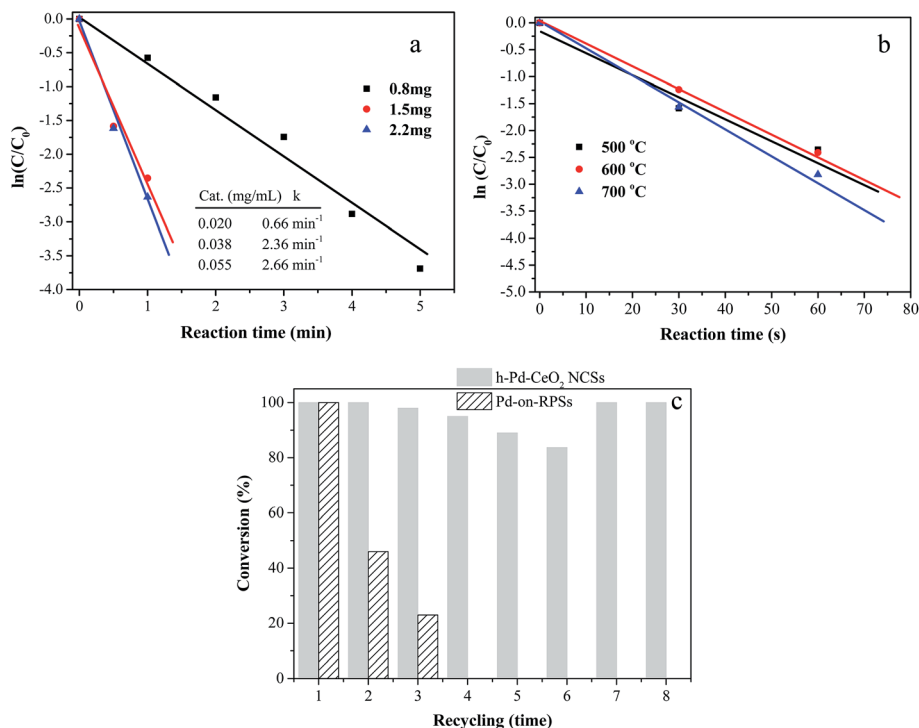


Fig. 8 Plots of $\ln(C/C_0)$ vs. the reaction time (*t*) over the hollow Pd–CeO₂ NCS catalyst (a) with 0.8–2.2 mg (calcined at 500 °C), (b) with 1.5 mg (calcined at 500–700 °C), and (c) the conversion of 4-NP (4 min) vs. recycling times over the h-Pd–CeO₂ NCSs calcined at 500 °C and Pd-on-resin polymer sphere (RPS) catalysts (1.5 mg) for the reduction of 4-NP to 4-AP by an excess of NaBH₄ under ambient conditions.

weight loss during the separation process rather than degradation of the catalyst, which is the reason for the decrease of the catalytic conversion with increasing recycling times.

Moreover, we prepared the catalyst of Pd NPs supported on resin polymer spheres (denoted as Pd-on RPSs), and its catalytic performance for the reduction of 4-NP to 4-AP by an excess of NaBH₄ under ambient conditions was tested. The results (Fig. 8c) show that after being repeatedly used 3 times, the catalytic activity of Pd-on RPSs decreases dramatically, probably due to the detachment of Pd NPs from the resin polymer spheres.

The Pd supported on CeO₂ is one of the most prevalent catalysts in the exhaust emission control, so the catalytic performance of the hollow Pd–CeO₂ NCS catalyst for CO oxidation was also evaluated. Typically, 30 mg of h-Pd–CeO₂ NCSs was loaded in a U-type quartz tubular reactor, the gas mixture of 1% CO–20% O₂/N₂ was used as the feed gas, and the space velocity was 100 000 mL g_{cat}⁻¹ h⁻¹.

As shown in Fig. 9a, the h-Pd–CeO₂ NCSs possess good catalytic activity for CO oxidation in a high space velocity of 100 000 mL g_{cat}⁻¹ h⁻¹, and the calcination temperature affects their catalytic activity, for instance, the sample calcined at 700 °C exhibits higher catalytic activity than the sample calcined at 500 or 600 °C. This situation is consistent with the catalytic reduction of 4-NP over this h-Pd–CeO₂ NCS catalyst, which should be attributed to the higher surface concentration of Pd species on the sample calcined at 700 °C (Table 1).

A cycling test was conducted to study the stability of the h-Pd–CeO₂ NCS catalyst at different temperatures, in which the reaction was tested at 600 °C for 30 min, and then the reaction temperature was cooled to 130 °C to evaluate the CO oxidation for 30 min, and then repeated the cycling operation mentioned above. As seen in Fig. 10, after the alternate reaction at 600 °C and 130 °C three times, the h-Pd–CeO₂ NCSs still maintain around 80% CO conversion at 130 °C. As shown in its TEM image (Fig. S11†), its original structure can be well retained after being used alternately at 600 °C and 130 °C three times, indicating its high and stable catalytic performance at higher reaction temperature.

The catalytic activities of the three Pd catalysts for CO oxidation are shown in Fig. 9b. The activity of the h-Pd–CeO₂ NCS catalyst is much higher than those of Pd/CeO₂-imp and the physical mixture of Pd + CeO₂ catalysts. Based on the differences in the textural and physicochemical properties of the three catalysts, the higher activity of the h-Pd–CeO₂ NCS catalyst for the CO oxidation might be closely related to the size of Pd NPs, the surface area of the catalyst and the interface between Pd and CeO₂.^{50–52} In the h-Pd–CeO₂ NCSs, the Pd NPs are uniformly scattered in the ceria shell and no aggregation occurs after calcination at high temperature. Besides, a comparatively higher surface area of h-Pd–CeO₂ NCSs would be beneficial to the improvement of its catalytic activity.

The larger Pd particles detached from the nanosized CeO₂ can be observed in the mixture of the Pd + CeO₂ catalyst, due to sintering at high temperature. For the Pd/CeO₂-imp catalyst, the



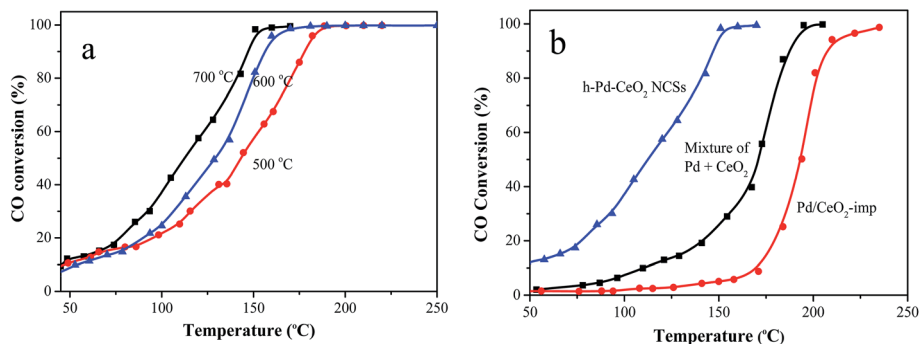


Fig. 9 CO oxidation over (a) h-Pd-CeO₂ NCSs calcined at 500–700 °C, and (b) h-Pd-CeO₂ NCSs, Pd/CeO₂-imp and the physical mixture of Pd + CeO₂ catalysts (space velocity of 100 000 mL g_{cat}⁻¹ h⁻¹).

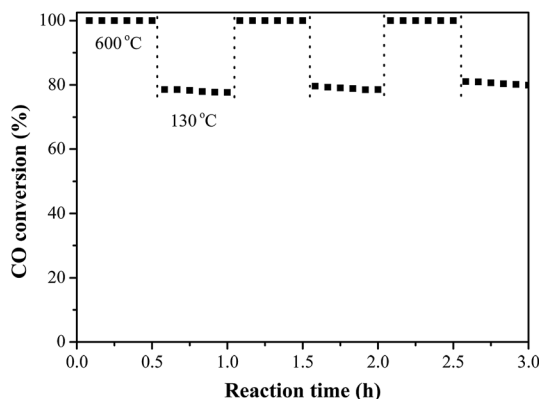


Fig. 10 CO oxidation over the h-Pd-CeO₂ NCS catalyst at alternate changes of 600 °C and 130 °C (space velocity of 100 000 mL g_{cat}⁻¹ h⁻¹).

surface area and TEM testing have confirmed a low surface area and uneven distribution of PdO particles on the sample. These disadvantages result in their poor catalytic activities at low temperature (below 120 °C).

In the h-Pd-CeO₂ NCSs, the electron exchange occurs at the interface between Pd NPs and nanosized CeO₂, and the surface Pd species is ionic, as evidenced in the Pd 3d XPS profile. To maintain the charge neutrality, the oxygen vacancies should be created at the CeO₂ near Pd NPs, leading to the partial reduction of CeO₂ to CeO_{2-x}, because of the lower valence state of Pd²⁺ compared to that of the Ce⁴⁺. Therefore, we can conclude that the Pd²⁺ ions at the interface are the active sites for CO adsorption, and the neighboring oxygen vacancies can facilitate the adsorption and activation of gaseous O₂ to form peroxide (O₂²⁻) species,⁵³ thus the CO oxidation could occur at lower temperature. And the O 1s XPS spectra in Fig. S12† clearly shows that the h-Pd-CeO₂ NCS has a higher ratio of surface chemisorbed oxygen (531.8 eV) to lattice oxygen (529.2 eV) than that of the supported Pd/CeO₂-imp catalyst. More chemisorbed oxygen species would be beneficial to the reaction with the absorbed CO molecules on nearby interfacial Pd²⁺ species, which could well improve the catalytic activity for the CO oxidation. After this catalyst was used in the CO oxidation, the valence state of Pd is mostly still in a form of ionic state (Fig. 6c).

Two new tiny peaks at EB = 335.3 eV and 340.5 eV in its Pd 3d XPS spectrum showed the formation of metallic Pd⁰ species, which might be caused by the reduction of CO.³⁹

4. Conclusions

In summary, we have successfully prepared hollow Pd-CeO₂ nanocomposite spheres (NCSs) *via* a polymer-template method. The Pd nanoparticles (NPs) in the feedstock solution are closely stacked in the surrounding CeO₂ nanocrystals after eliminating the template core, that is to say, the Pd NPs are highly dispersed inside the CeO₂ shell in these prepared hollow Pd-CeO₂ NCS materials, and would not aggregate even after being calcined at 700 °C and their structure and catalytic performance could be well maintained. The confined shield effect of the CeO₂ shell can efficiently inhibit the aggregation of Pd NPs and prevents the leaching of Pd species in the solution reaction. Besides, the surface Pd species in the hollow Pd-CeO₂ NCSs is mainly ionic, which is caused by the electron exchange between Pd atoms and their surrounding CeO₂ nanocrystals in the calcination process. Therefore, the synergistic catalytic effect between Pd NPs and CeO₂ can be enhanced in this core-shell like structure.

For the aqueous-phase selective reduction of 4-nitrophenol to 4-aminophenol and gas phase low temperature oxidation of CO, this hollow Pd-CeO₂ NCS material shows excellent catalytic activity and reusability, compared to that of the supported Pd/CeO₂ catalyst and the physically mixed catalyst of Pd + CeO₂. The synthetic strategy herein might provide a novel guidance for the designing and fabrication of multi-core@oxide shell core-shell nanocomposites that can act as effective multifunctional nanoreactors in a variety of research fields.

Acknowledgements

This project was financially supported by the National Natural Science Foundation of China (21273150), the National Basic Research Program of China (2013CB933201), the National High Technology Research and Development Program of China (2011AA03A406, 2012AA062703), and the Fundamental Research Funds for the Central Universities.



References

- 1 K. Serp and K. Philippot, *Nanomaterials in Catalysis*, Wiley-VCH, 2012.
- 2 D. Astruc, F. Lu and J. R. Aranzas, *Angew. Chem., Int. Ed.*, 2005, **44**, 7852–7872.
- 3 W. Yu, M. D. Porosoff and J. G. Chen, *Chem. Rev.*, 2012, **112**, 5780–5817.
- 4 G. H. Hutchings and C. J. Kiely, *Acc. Chem. Res.*, 2013, **46**, 1759–1772.
- 5 S. Linic, P. Christopher, X. Hong and A. Marimuthu, *Acc. Chem. Res.*, 2013, **46**, 1890–1899.
- 6 Y. Xia, X. Xia, Y. Wang and S. Xie, *MRS Bull.*, 2013, **38**, 335–344.
- 7 Q. L. Zhu, J. Li and Q. Xu, *J. Am. Chem. Soc.*, 2013, **135**, 10210–10213.
- 8 T. W. Hansen, A. T. DeLaRiva, S. R. Shalla and A. K. Dayte, *Acc. Chem. Res.*, 2013, **46**, 1720–1730.
- 9 R. Ouyang, J. Liu and W. Li, *J. Am. Chem. Soc.*, 2013, **135**, 1760–1771.
- 10 M. Pérez-Lorenzo, B. Vaz, V. Salgueiriño and M. A. Correa-Duarte, *Chem.-Eur. J.*, 2013, **19**, 12196–12211.
- 11 H. C. Zeng, *Acc. Chem. Res.*, 2013, **46**, 226–235.
- 12 Y. Deng, Y. Cai, Z. Sun, J. Liu, C. Liu, J. Wei, W. Li, C. Liu, Y. Wang and D. Zhao, *J. Am. Chem. Soc.*, 2010, **132**, 8466–8473.
- 13 J. Ge, Q. Zhang, T. Zhang and Y. Yin, *Angew. Chem., Int. Ed.*, 2008, **47**, 8924–8928.
- 14 Y. Dai, B. Lim, Y. Yang, C. M. Copley, W. Li, E. C. Cho, B. Grayson, P. T. Fanson, C. T. Campbell, Y. Sun and Y. Xia, *Angew. Chem., Int. Ed.*, 2010, **49**, 8165–8168.
- 15 P. Lu, C. T. Campbell and Y. Xia, *Nano Lett.*, 2013, **13**, 4957–4962.
- 16 Q. Zhang, I. Lee, J. B. Joo, F. Zaera and Y. Yin, *Acc. Chem. Res.*, 2013, **46**, 1816–1824.
- 17 G. Li and Z. Tang, *Nanoscale*, 2014, **6**, 3995–4011.
- 18 J. Lu, B. Fu, M. C. Kung, G. Xiao, J. W. Elam, H. H. Kung and P. C. Stair, *Science*, 2012, **335**, 1205–1208.
- 19 L. Shang, T. Bian, B. Zhang, D. Zhang, L. Wu, C. Tung, Y. Yin and T. Zhang, *Angew. Chem., Int. Ed.*, 2014, **53**, 250–254.
- 20 Z. Sun, H. Zhang, Y. Zhao, C. Huang, R. Tao, Z. Liu and Z. Wu, *Langmuir*, 2011, **27**, 6244–6251.
- 21 C. T. Campbell, *Nat. Chem.*, 2012, **4**, 597–598.
- 22 A. Bruix, J. A. Rodriguez, P. J. Ramirez, S. D. Senanayake, J. Evans, J. B. Park, D. Stacchiola, P. Liu, J. Hrbek and F. Illas, *J. Am. Chem. Soc.*, 2012, **134**, 8968–8974.
- 23 P. Hu, Z. Huang, Z. Amghouz, M. Makkee, F. Xu, F. Kapteijn, A. Dikhtiarenko, Y. Chen, X. Gu and X. Tang, *Angew. Chem., Int. Ed.*, 2014, **53**, 3418–3421.
- 24 N. Ta, J. Liu, S. Chenna, P. A. Crozier, Y. Li, A. Chen and W. Shen, *J. Am. Chem. Soc.*, 2012, **134**, 20585–20588.
- 25 J. Paier, C. Penshke and J. Sauer, *Chem. Rev.*, 2013, **113**, 3949–3985.
- 26 N. Acerbi, S. Golunski, S. H. Tsang, H. Daley, C. Hardacre, R. Smith and P. Collier, *J. Phys. Chem. C*, 2012, **116**, 13569–13583.
- 27 C. Sun, H. Li and L. Chen, *Energy Environ. Sci.*, 2012, **5**, 8475–8505.
- 28 Y. Jiao, F. Wang, X. Ma, Q. Tang, K. Wang, Y. Guo and L. Yang, *Microporous Mesoporous Mater.*, 2013, **176**, 1–7.
- 29 N. C. Strandwitz and G. D. Stucky, *Chem. Mater.*, 2009, **21**, 4577–4582.
- 30 C. Y. Cao, Z. M. Cui, C. Q. Chen, W. G. Song and W. Cai, *J. Phys. Chem. C*, 2010, **114**, 9865–9870.
- 31 B. Liu, S. Yu, Q. Wang, W. Hu, P. Jing, Y. Liu, W. Jia, Y. Liu, L. Liu and J. Zhang, *Chem. Commun.*, 2013, **49**, 3757–3759.
- 32 N. Zhang and Y. J. Xu, *Chem. Mater.*, 2013, **25**, 1979–1988.
- 33 J. Liu, S. Z. Qiao, H. Liu, J. Chen, A. Orpe, D. Zhao and G. Q. Lu, *Angew. Chem., Int. Ed.*, 2011, **50**, 5947–5951.
- 34 T. Teranishi and M. Miyake, *Chem. Mater.*, 1998, **10**, 594–600.
- 35 S. Guo, S. Dong and E. Wang, *ACS Nano*, 2010, **4**, 547–555.
- 36 H. Sun, J. He, J. Wang, S. Y. Zhang, C. Liu, T. Sritharan, S. Mhaisalkar, M. Y. Han, D. Wang and H. Chen, *J. Am. Chem. Soc.*, 2013, **135**, 9099–9110.
- 37 K. Noack, H. Zbinden and R. Schlögl, *Catal. Lett.*, 1990, **4**, 145–155.
- 38 S. Hinokuma, H. Fujii, M. Okamoto, K. Ikeue and M. Machida, *Chem. Mater.*, 2010, **22**, 6183–6190.
- 39 K. R. Priolkar, P. Bera, P. R. Sarode, M. S. Hegde, S. Emura, R. Kumashiro and N. P. Lalla, *Chem. Mater.*, 2002, **14**, 2120–2128.
- 40 M. S. Hegde, G. Madras and K. C. Patil, *Acc. Chem. Res.*, 2009, **42**, 704–712.
- 41 B. Basu, S. Das, P. Das, B. Mandal, D. Banerjee and F. Almqvist, *Synthesis*, 2009, **7**, 1137–1146.
- 42 B. Basu and S. Paul, *Appl. Organomet. Chem.*, 2013, **27**, 588–594.
- 43 S. Zhang, C. Chen, M. Cargnello, P. Fornasiero, R. J. Gorte, G. W. Graham and X. Pan, *Nat. Commun.*, 2015, **6**, 7778–7784.
- 44 G. J. Wang, Y. Guo and G. Z. Lu, *Fuel Process. Technol.*, 2015, **130**, 71–77.
- 45 S. Praharaj, S. Nath, S. K. Ghosh, S. Kundu and T. Pal, *Langmuir*, 2004, **20**, 9889–9892.
- 46 T. Yu, J. Zeng, B. Lim and Y. Xia, *Adv. Mater.*, 2010, **22**, 5188–5192.
- 47 X. Liu, X. Bian, G. Nie, C. Zhang, C. Wang and Y. Wei, *J. Mater. Chem.*, 2012, **22**, 12723–12730.
- 48 Y. Mei, Y. Liu, F. Polzer, M. Ballauff and M. Drechsler, *Chem. Mater.*, 2007, **19**, 1062–1069.
- 49 H. Li, L. Han, J. Cooper-White and I. Kim, *Green Chem.*, 2012, **14**, 586–591.
- 50 A. I. Boronin, E. M. Slavinskaya, I. G. Danilova, R. V. Gulyaev, Y. I. Amosov, P. A. Kuznetsov, I. A. Polukhina, S. V. Koscheev, V. I. Zaikovskii and A. S. Noskov, *Catal. Today*, 2009, **144**, 201–211.
- 51 R. V. Gulyaev, A. I. Stadnichenko, E. M. Slavinskaya, A. S. Ivanova, S. V. Koscheev and A. I. Boronin, *Appl. Catal., A*, 2012, **439**, 41–50.
- 52 M. Cargnello, V. V. T. Doan-Nguyen, T. R. Gordon, R. E. Diaz, E. A. Starch, R. J. Gorte, P. Fornasiero and C. B. Murray, *Science*, 2013, **341**, 771–773.
- 53 H. Y. Li, H. F. Wang, X. Q. Gong, Y. L. Guo, Y. Guo, G. Z. Lu and P. Hu, *Phys. Rev. B: Condens. Matter Mater. Phys.*, 2009, **79**(19), 193401–193404.

